Faraday Discussions
Cite this: DOI: 10.1039/d6fd00006a

ROYAL SOCIETY OF CHEMISTRY

PAPER

View Article Online
View Journal

Rare earth ion transport and selectivity in large diameter nanotube porins

Jobaer Abdullah, [ab] Zhongwu Li, [a] Yuhao Li [a] and Aleksandr Noy *[ab]

Received 13th January 2026, Accepted 6th February 2026
DOI: 10.1039/d6fd00006a

Selective separation of rare earth elements (REEs) in nanoporous media is very challenging due to the similar physicochemical properties of lanthanide ions. In this work, we systematically investigate the transport and selectivity of REE^{3+} ions through two model nanofluidic channels: 1.5 nm diameter carbon nanotube porins (wCNTPs) and 2.1 nm diameter boron nitride nanotube porins (BNNTPs). Using a fluorescence-based vesicle assay, we find that wCNTPs show almost no differential selectivity across the lanthanide series, a behavior consistent with bulk-dominant transport through their moderately-confined channels with chemically inert, hydrophobic walls. In contrast, BNNTPs exhibit nearly an order of magnitude higher permeability and mild differential selectivity, following a volcano-shaped trend with Eu^{3+} ions showing the highest permeability. We attribute this enhanced performance to the high negative surface charge of BNNTPs, which facilitates a surface-dominated transport mechanism where ion migration within the electric double layer becomes the primary contributor to ion transport. These results elucidate the distinct roles of surface charge in nanoscale confinement and provide critical design rules for the development of future membranes tailored for efficient REE separations.

1 Introduction

Membrane separations have become indispensable to modern industrial technologies,[1] with sophisticated polymer membranes powering applications such as water treatment and desalination,[2] gas separation,[3] and hemodialysis.[4] Yet biological membranes, which rely on specialized protein channels to support the machinery of life, still represent a gold standard of transport and separation efficiency and precision.[5,6] In these biological systems, pore transport properties are not merely a function of its size, but are tightly regulated by the precise structure, geometry, and chemical properties of the channel walls. Synthetic nanofluidic channels provide a convenient, simplified model of these complex

[a]Physical and Life Sciences Directorate, Lawrence Livermore National Laboratory, Livermore, CA 94550, USA. E-mail: noy1@llnl.gov
[b]School of Natural Sciences, University of California Merced, Merced, CA 95343, USA

biological pores, allowing researchers to isolate and explore key physical phenomena that emerge under extreme spatial confinement. Recent studies utilizing these platforms have revealed fluid behaviors that defy continuum expectations, such as drastic changes in the dielectric properties of confined water, unusual ion selectivity, ultra fast transport in carbon nanotubes, and quantum friction in graphene channels.[7–9]

High spatial confinement, in particular, amplifies the role and impact of the channel surface on transport dynamics. As the channel dimensions approach the Debye screening length or the molecular scale of the fluid itself, the physicochemical nature of the interface begins to dominate the transport physics.[7–9] Depending on the specific wall chemistry and electronic structure, this confinement can lead to divergent behaviors. For instance, smooth, hydrophobic surfaces can induce high slip flow, where friction is minimized, leading to flow rates that far exceed hydrodynamic predictions.[10,11] Conversely, highly charged walls can amplify the role of surface-governed transport, where the migration of counterions within the electric double layer becomes the primary contributor to the overall channel conductance.[7,12]

Here, we explore the impact of these distinct transport mechanisms, as well as the influence of surface charge and chemistry, by comparing two model channels

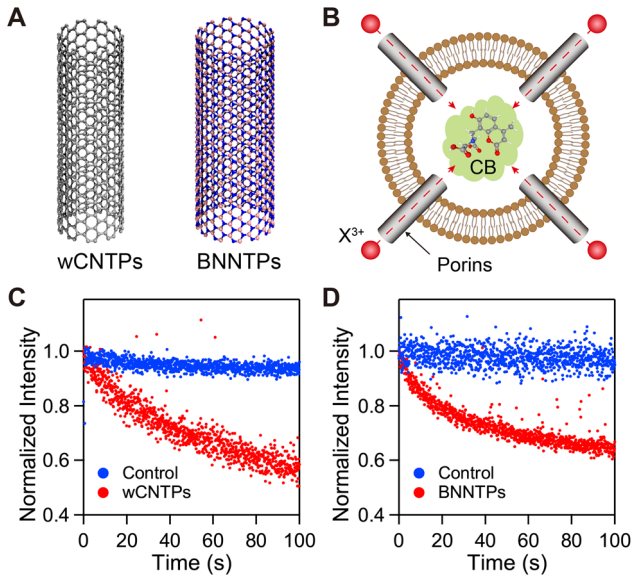

Fig. 1 Rare earth ion transport kinetics in model nanotube porin channels. (A) Structures of 1.5 nm diameter carbon nanotube porin (wCNTP, left) and 2.1 nm diameter boron nitride nanotube porin (BNNTP, right). Nanotube porin length distributions center at 13.4 nm for wCNTPs,[15,16] and at 38.4 nm for BNNTPs.[14] (B) Schematics of the ion transport measurement experiment where a REE ion sensitive dye, Calcein Blue (CB), was encapsulated inside lipid vesicles. (C) CB fluorescence intensity kinetics recorded after exposure to a REE ion gradient in the presence (red) and absence (blue) of the CNTP channels in the vesicle membrane. (D) CB fluorescence intensity kinetics recorded after exposure to a REE ion gradient in the presence (red) and absence (blue) of the BNNTP channels in the vesicle membrane.

that implement moderate spatial confinement (Fig. 1A): 1.5 nm wide single-wall carbon nanotube porins (wCNTPs)[13] and 2.1 nm double-wall boron nitride nanotube porins (BNNTPs).[14] While these two scaffolds share a similar overall structure and smooth channel wall geometry, they possess fundamentally different electronic and chemical properties. wCNTPs are characterized by hydrophobic, chemically inert walls that facilitate high slip,[8] but interact weakly with ions. In contrast, BNNTPs feature smooth but highly charged walls.[12] In this work, we measure the transport rates and differential selectivity of both channels for a series of rare earth element (REE) cations, which serve as critical resources for modern technologies, yet remain difficult to separate due to their similar physicochemical properties.

Our results show that while both channels support REE ion transport, their performance characteristics differ significantly. wCNTPs demonstrate moderately efficient REE ion transport but exhibit almost no differential selectivity across the lanthanide series. This behavior is consistent with the properties of chemically inert walls and high slip, which, in the absence of strong surface interactions, lead to a prevalently bulk-dominant mode of ion transport. BNNTPs, on the other hand, exhibit almost an order of magnitude higher transport efficiency and much higher differential selectivity across the REE ion series. We attribute these enhanced properties to the role of the highly charged BNNT walls, which support efficient surface transport mechanism. This surface-dominated regime allows the BNNTPs to discriminate between ions based on subtle differences in hydration and electrostatic interactions. These results elucidate the distinct roles of slip and surface charge in nanofluidic transport and point to critical design rules for future membranes tailored for efficient REE ion separations.

2 Results and discussion

2.1 Ion transport in CNTPs and BNNTPs

To assess ion transport through CNTPs, we designed a vesicle-based assay that exploited quenching of an organic water-soluble fluorescent dye Calcein Blue (CB) by REE^{3+} ions. We chose CB for this assay because it has the highest quenching capacity among the lanthanide-sensitive dyes.[17] We synthesized wCNTPs by sonication-assisted cutting of the purified stock of macroscopic length CNTs in presence of lipid surfactant using a previously reported protocol.[15] We fabricated BNNTPs by applying a similar lipid-assisted sonochemical cutting method to dice up macroscopically long double-walled BNNTs, following a previously reported protocol.[14] For the rare earth ion permeability assay we have incorporated nanotube porins into the walls of large unilamellar lipid vesicles that also encapsulated CB dye solution (Fig. 1A and B, also see the Methods section for details).

We conducted our experiments at pH = 8 to maximize the REE detection sensitivity of the CB dye. At this mildly basic pH rare earth ions undergo partial hydrolysis with roughly 30–60% of REE^{3+} ions existing as $REE(OH)^{2+}$ ions (see Table 1 for speciation details). At the concentration range of our experiments, we did not observe any lanthanide hydroxide precipitation on the timescale of our kinetics measurements. Hydrolysis of REE^{3+} ions to $REE(OH)^{2+}$ leads to a modest reduction in the effective hydrated diameter (*ca.* 0.2–0.5 Å) as a result of decreased coordination number and contraction of the first hydration shell.[18,19] While such

Table 1 REE(III) speciation at pH 8 as percentage of the overall REE amount

Ion	REE^{3+}	$REE(OH)^{2+}$	$REE(OH)_2^{+}$	$REE(OH)_3$ (aq)
Ce^{3+}	65.4	32.0	2.5	<0.01
Nd^{3+}	55.2	40.7	4.0	<0.1
Eu^{3+}	37.8	56.5	5.6	0.01
Gd^{3+}	49.7	47.2	3.1	0.01
Yb^{3+}	33.2	58.6	8.1	0.1

differences can influence dehydration barriers and ion transport under extreme sub-nanometer confinement, their impact is expected to be minimal in the present system, where the channel diameters (1.5 nm and 2.1 nm) are larger than the hydrated ion size for both ions. For simplicity, we refer to the rare earth ions that we studied as REE^{3+} for the remainder of this manuscript, unless we specifically discuss the differences between their REE^{3+} and $REE(OH)^{2+}$ ion forms.

To measure rare earth ion transport kinetics, we initiated a concentration gradient of REE^{3+} ions across the vesicle wall by rapidly mixing the vesicle solution with lanthanide ion solution in the fluorescence spectrometer cuvette and monitoring the CB fluorescence (Fig. 1B). As expected, pure lipid vesicles were impermeable to REE^{3+} ions in the absence of CNTPs or BNNTPs (Fig. 1C and D). In contrast, the presence of wCNTP or BNNTP channels in the vesicle walls led to a pronounced decrease in CB fluorescence (Fig. 1C and D), indicating that REE^{3+} rapidly translocated into the vesicle interior through the nanotube porin channels. Measurements performed at varying REE ion concentrations (0.25–1.25 mM for wCNTP transport experiments and 10–50 μM for BNNTP transport experiments), revealed a linear dependence of ion flux on the REE^{3+} concentration gradient, which was then used to calculate the vesicle permeability (see Materials and methods for details).

Our ion transport measurement results show the unitary channel permeability of wCNTP value for Eu^{3+} ions as $(1.75 \pm 0.12) \times 10^{-20}$ cm^3 s^{-1}, which was very low (Fig. 2B). This value is several orders of magnitude lower than the unitary channel permeability for monovalent K^+ ions (Fig. 2A). The much smaller permeability for REE^{3+} ions relative to K^+ ions is not surprising. Trivalent lanthanide ions and their

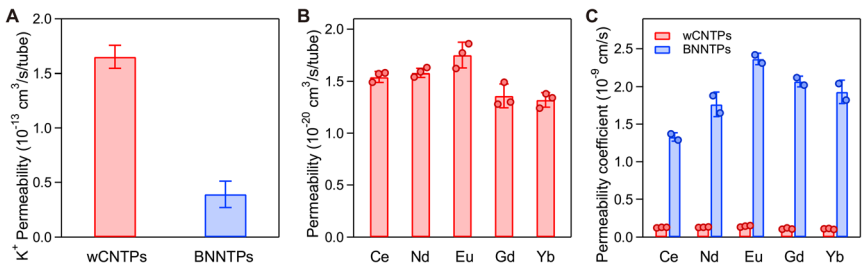

Fig. 2 Ion transport in CNTP and BNNTP channels. (A) K^+ ion permeability of individual CNTP and BNNTP channels, calculated from the corresponding single-channel ion conductance values using the Nernst–Einstein ratio.[13,14] (B) Rare earth ion permeability of CNTP channels. Error bars: SD. (C) Comparison of rare earth ion permeability of vesicles containing CNTP (red bars) and BNNTP (blue bars) channels. Error bars: SD.

monohydroxylated forms have high charge density and a strongly bound hydration shell. The diameter of this tightly bound first hydration shell (0.47–0.51 nm),[20] is still much smaller than the inner wCNTP diameter, indicating that the dehydration barriers cannot impose a significant energy penalty on the ion transport. Still, the strong confinement that this bulky hydrated ion encounters inside the wCNTP channel hinders its transport and can lead to a significant reduction in diffusion efficiency.[21] We also observed qualitatively similar transport behavior for five different lanthanide ions that we tested (Fig. 2B). These results demonstrate that REE^{3+} ion permeation through wCNTP channels is a general phenomenon and is not restricted to a specific lanthanide such as Eu^{3+}.

Surprisingly, when we measured the lanthanide ions permeability in BNNTPs using a similar vesicle based assay, BNNTPs showed one order of magnitude higher permeability than wCNTPs (Fig. 2C). Even though BNNTPs have slightly larger diameter than wCNTPs, they are also significantly longer (the peak of length distribution of wCNTPs is at 13.4 nm (ref. 15 and 16) *versus* 38.4 nm for BNNTPs[14]); therefore we expect the pure differences in geometry to produce *ca.* 30% reduction in ion flux. We cannot attribute the lanthanide ion transport enhancement in BNNTPs to those geometrical differences; instead, we argue that this higher transport rate originates from the different surface chemistry of those nanochannels.

Unlike CNTPs, BNNTPs have a strong negative charge on their walls,[12,14] which raises the possibility of surface transport making a strong contribution to the overall transport efficiency. Indeed, we would expect that trivalent REE^{3+} cations, as well as the divalent $REE(OH)^{2+}$ cations, would be strongly attracted to these negatively charged BNNT walls and form a strongly bound surface layer of counterions. It is this layer that supports efficient surface diffusion that in turn contributes to the higher permeability of the BNNTP channels relative to their wCNTP analogs.

2.2 Surface and bulk transport in CNTPs and BNNTPs

A more quantitative analysis supports this conclusion. The balance between the surface and bulk conductance contributions in nanofluidic transport is characterized by the Dukhin number, Du, given as:[7,22]

$$\mathrm{Du} = \frac{\Sigma}{h \times eN_a C_0} \tag{1}$$

where h is the channel size (diameter in the case of nanotube porins), C_0 is the electrolyte concentration, N_a is the Avogadro number, and e is the electron charge. Previous works have estimated the surface charges on the BNNTP and CNTP surfaces as -230 mC m^{-2} and -1 mC m^{-2}, respectively,[13,14] which result in the Du values of 11.4 for BNNTPs and 0.7 for CNTPs. The much higher value for BNNTPs, which falls into the Du $\gg$ 1 range, confirms our conclusion that surface transport plays a dominant role in these channels. In contrast, the Du < 1 value for CNTPs indicates that surface transport plays a much less important role in ion transport in those channels.

2.3 Lanthanide ion transport selectivity in CNTPs and BNNTPs

These differences in the mechanism of ion transport are also reflected in the differential transport selectivity of these channels across the lanthanide series. wCNTPs, which are dominated by bulk mode of transport and chemically-inert

low surface charge walls, show almost no differential selectivity for different lanthanide ions (Fig. 2B). In contrast, BNNTPs show noticeable selectivity when tested with the same ion series (Fig. 2C). The permeability follows a volcano-shaped selectivity trend, with Eu^{3+} exhibiting the highest permeability and Ce^{3+} showing the lowest permeability. This behavior is qualitatively consistent with lanthanide transport selectivity trends observed in other channels with high surface charge, such as MoS_2.[23] However, unlike our nanopores, those channels were narrower, thus requiring partial dehydration of the ions upon entry. As the result, their selectivity trend was attributed to a balance between the value of the dehydration energy and the inter-channel diffusion barrier. Our results indicate that even in cases where ion dehydration is not sufficient, strong binding to the channel walls and subsequent diffusion along them could lead to a similar differential selectivity trend. We have also investigated potential correlation of the differential selectivity data with the REE ion speciation, but saw only very weak correlations that did not change our interpretation of the data. Further modeling and experimental investigations of microscopic mechanisms of ion transport in these channels at different pH values should clarify the origins of this behavior and address any preferences for a particular hydroxylated ion form. Overall, our data point to the importance of harnessing the surface transport mechanism for selective separations and provide additional clues for efficient design of membranes for future precision separations.

3 Materials and methods

3.1 Materials and chemicals

1,2-Dioleoyl-*sn*-glycero-3-phosphocholine (DOPC) lipid was purchased from Avanti Polar Lipids and used as received. Lanthanide chlorides were obtained from Sigma-Aldrich and dissolved in deionized water for use in the experiments. Calcein Blue dye was also purchased from Sigma-Aldrich and prepared as an aqueous solution.

3.2 wCNTP fabrication

wCNTPs were synthesized and purified following a previously reported protocol.[15,24] Briefly, the CNT bundles were dispersed in DOPC lipids, bath-sonicated to separate them into individual nanotubes, followed by prolonged microtip sonication to generate ultrashort wCNTPs.

3.3 BNNTP fabrication

BNNTPs were synthesized following a previously reported protocol,[14] adapted from the established protocols for CNTP synthesis.

3.4 wCNTP incorporation into liposomes

DOPC lipid dissolved in chloroform was aliquoted (1 mg) into glass vials, and the solvent was removed under a gentle stream of air followed by further drying in a vacuum desiccator for over 12 hours. To incorporate wCNTPs into liposomes, 0.5 mL of the wCNTP solution was similarly dried under vacuum to eliminate residual solvent. The resulting wCNTP film was rehydrated with 1 mL of buffer solution (10 mM Tris and 80 mM NaCl, adjusted to pH 8.0) and subsequently used

to hydrate the pre-dried lipid film. For control samples, 2 mg of DOPC was used in place of wCNTPs. The lipid suspensions were hydrated at room temperature for 30 minutes and then subjected to seven freeze–thaw cycles by alternately flash-freezing in liquid nitrogen and thawing at 50 °C. Large unilamellar vesicles (LUVs) or wCNTP-LUVs were formed by extruding the suspensions 21 times through a 200 nm polycarbonate membrane using a mini-extruder (Avanti Polar Lipids). Excess dye external to the vesicles was removed by size-exclusion chromatography using a Sepharose CL-6B column. The average hydrodynamic diameter of the vesicles was determined by dynamic light scattering using a Zetasizer Nano-ZS90 (Malvern Instruments).

3.5 BNNTP incorporation into liposomes

BNNTP-LUVs were formed using the same procedure used for wCNTPs.

3.6 Calibration of REE^{3+} ion sensitivity of Calcein Blue dye

We have monitored the fluorescence intensity of the Calcein Blue dye emission peak at 440 nm using 370 nm wavelength for the excitation light. To calibrate the REE^{3+} response of the CB dye, we mixed the 0.15 mM CB dye solution with a series of known REE^{3+} concentrations. The relationship between the relative quenching efficiency expressed as $(I_0 - I)/I$, reflecting the fractional decrease in fluorescence upon REE^{3+} addition, and REE^{3+} concentration (C) was then described by the following empirical formula, with the values of the exponent pow falling into the range of 0.56 > pow > 0.36 for different REE^{3+} ions:

$$C = y_0 + A\left(\frac{I_0 - I}{I}\right)^{\text{pow}} \tag{2}$$

3.7 Ion permeability measurements

The lanthanide ions' permeability measurements were carried out using a spectrofluorometer using the same excitation wavelength of 370 nm and emission wavelength of 440 nm combination used for the CB dye calibration. In a typical experiment, 1900 μL of buffer (10 mM Tris and 80 mM NaCl, adjusted to pH 8.0) and 100 μL of LUVs containing 3 mM CB dye solution were added to a cuvette and placed in the spectrofluorometer. After introducing 5 μL of the REE solution, we recorded the kinetics of the fluorescence decrease caused by CB quenching by lanthanide ions. These kinetic curves were then used to calculate the REE flux, using the following equation:

$$J_x = \frac{V}{S} \times \frac{\mathrm{d[Q]}}{\mathrm{d}t} \tag{3}$$

where S and V are surface area and volume of vesicles. $\frac{\mathrm{d[Q]}}{\mathrm{d}t}$ is the initial slope of the kinetic curve. These data were collected for at least 5 different concentration gradients, and the vesicle ion permeability was calculated from the slope of the plot of ion flux as a function of the concentration gradient:

$$P = \frac{J_x}{\Delta C} \tag{4}$$

4 Conclusions

In this work, we systematically investigated the transport and selectivity of trivalent lanthanide ions through two model nanofluidic channels—1.5 nm wCNTPs and 2.1 nm BNNTPs—to elucidate how nanoscale confinement and surface chemistry govern ion transport. Using a fluorescence-based vesicle assay, we demonstrated that both channel types permit lanthanide ion transport, but with markedly different efficiencies and selectivities. wCNTPs exhibited relatively low permeability and negligible selectivity across the lanthanide series, consistent with a bulk-dominated transport regime arising from their hydrophobic, chemically inert, and weakly charged walls. In contrast, BNNTPs showed nearly an order of magnitude higher permeability and pronounced differential selectivity, following a volcano-shaped trend with Eu^{3+} displaying the highest permeability. Quantitative analysis confirmed that transport in BNNTPs is dominated by surface conduction, enabled by their high negative surface charge, which promotes strong electrostatic interactions and ion migration along the channel walls. These findings highlight the critical role of surface charge in enabling surface-dominated transport and ion discrimination even in relatively wide nanopores where dehydration effects are minimal. Overall, our findings provide mechanistic insights into transport mechanisms in larger diameter nanotube porins and establish key design principles for developing next-generation nanofluidic membranes tailored for efficient and selective rare earth element separations.

Author contributions

Aleksandr Noy: conceptualization, resources, funding acquisition, supervision, writing – review and editing; Jobaer Abdullah: experimental measurements, data analysis, writing – original draft; Zhongwu Li and Yuhao Li: data analysis, protocol development, writing – review and editing.

Conflicts of interest

There are no conflicts to declare.

Data availability

All data needed to evaluate the conclusions are presented in the paper. All data presented in this work have also been deposited to Figshare and are available at DOI: https://doi.org/10.6084/m9.figshare.31046713.

Acknowledgements

We thank the anonymous reviewer for helpful comments. wCNTP and BNNTP synthesis and characterization were supported as part of the Center for Enhanced Nanofluidic Transport (CENT), an Energy Frontier Research Center funded by the US Department of Energy, Office of Science, Basic Energy Sciences under award number DE-SC0019112. Rare earth ion transport studies were supported by the LDRD program at LLNL under an award 24-ERD-016. Work at the Lawrence

Livermore National Laboratory was performed under the auspices of the US Department of Energy under Contract DE-AC5207NA27344.

References

1 D. S. Sholl and R. P. Lively, *Nature*, 2016, **532**, 435–437.
2 M. Shannon, P. Bohn, M. Elimelech, J. Georgiadis, B. Marinas and A. Mayes, *Nature*, 2008, **452**, 301–310.
3 W. J. Koros and G. Fleming, *J. Membr. Sci.*, 1993, **83**, 1–80.
4 M. K. van Gelder, S. M. Mihaila, J. Jansen, M. Wester, M. C. Verhaar, J. A. Joles, D. Stamatialis, R. Masereeuw and K. G. F. Gerritsen, *Expert Rev. Med. Devices*, 2018, **15**, 323–336.
5 R. J. Gilbert, H. Bayley and G. Anderluh, *Philos. Trans. R. Soc., B*, 2017, **372**, 20160208.
6 Y.-x. Shen, P. O. Saboe, I. T. Sines, M. Erbakan and M. Kumar, *J. Membr. Sci.*, 2014, **454**, 359–381.
7 L. Bocquet and E. Charlaix, *Chem. Soc. Rev.*, 2010, **39**, 1073–1095.
8 Z. Li and A. Noy, *Chem. Soc. Rev.*, 2025, **54**, 8582–8635.
9 Y. You, A. Ismail, G.-H. Nam, S. Goutham, A. Keerthi and B. Radha, *Annu. Rev. Mater. Res.*, 2022, **52**, 189–218.
10 S. Joseph and N. R. Aluru, *Nano Lett.*, 2008, **8**, 452–458.
11 R. Tunuguntla, R. Henley, Y.-C. Yao, T. A. Pham, M. Wanunu and A. Noy, *Science*, 2017, **357**, 792–796.
12 A. Siria, P. Poncharal, A.-L. Biance, R. Fulcrand, X. Blase, S. T. Purcell and L. Bocquet, *Nature*, 2013, **494**, 455–458.
13 Y.-C. Yao, A. Taqieddin, M. A. Alibakhshi, M. Wanunu, N. R. Aluru and A. Noy, *ACS Nano*, 2019, **13**, 12851–12859.
14 Z. Li, A. T. Hall, Y. Wang, Y. Li, D. O. Byrne, L. R. Scammell, R. R. Whitney, F. I. Allen, J. Cumings and A. Noy, *Sci. Adv.*, 2024, **10**, eado8081.
15 R. H. Tunuguntla, A. Escalada, V. A. Frolov and A. Noy, *Nat. Protoc.*, 2016, **11**, 2029–2047.
16 J. Geng, K. Kim, J. Zhang, R. Tunuguntla, L. Comolli, F. Allen, K. Cho, D. Munoz, Y. Wang, C. Grigoropoulos, C. Ajo-Franklin and A. Noy, *Nature*, 2014, **514**, 612–615.
17 H. G. Brittain, *Anal. Chem.*, 1987, **59**, 1122–1125.
18 W. W. Rudolph and G. Irmer, *J. Solution Chem.*, 2020, **49**, 316–331.
19 R. C. Shiery, J. L. Fulton, M. Balasubramanian, M.-T. Nguyen, J.-B. Lu, J. Li, R. Rousseau, V.-A. Glezakou and D. C. Cantu, *Inorg. Chem.*, 2021, **60**, 3117–3130.
20 Y. Marcus, *Chem. Rev.*, 1988, **88**, 1475–1498.
21 Z. Li, R. P. Misra, Y. Li, Y.-C. Yao, S. Zhao, Y. Zhang, Y. Chen, D. Blankschtein and A. Noy, *Nat. Nanotechnol.*, 2023, **18**, 177–183.
22 S. S. Dukhin, *Adv. Colloid Interface Sci.*, 1993, **44**, 1–134.
23 M. Wang, Q. Xiong, M. Wang, N. H. C. Lewis, D. Ying, G. Yan, E. Hoenig, Y. Han, O.-S. Lee, G. Peng, H. Zhou, G. C. Schatz and C. Liu, *Sci. Adv.*, 2024, **10**, eadh1330.
24 Y. Li, Z. Li, R. P. Misra, C. Liang, A. J. Gillen, S. Zhao, J. Abdullah, T. Laurence, J. A. Fagan and N. Aluru, *Nat. Mater.*, 2024, **23**, 1123–1130.